AIP Advances

Modeling inter-particle magnetic correlations in magnetite nanoparticle assemblies using x-ray magnetic scattering data

Cite as: AIP Advances **9**, 035033 (2019); https://doi.org/10.1063/1.5080155
Submitted: 06 November 2018 . Accepted: 31 January 2019 . Published Online: 19 March 2019

Johnathon Rackham, Brittni Newbold, Steve Kotter, Dallin Smith, Dalton Griner, Roger Harrison, Alex H. Reid, Mark Transtrum, and Karine Chesnel

Modeling inter-particle magnetic correlations in magnetite nanoparticle assemblies using x-ray magnetic scattering data

Cite as: AIP Advances 9, 035033 (2019); doi: 10.1063/1.5080155
Presented: 15 January 2019 • Submitted: 6 November 2018 •
Accepted: 31 January 2019 • Published Online: 19 March 2019

Johnathon Rackham,[1] Brittni Newbold,[1] Steve Kotter,[1] Dallin Smith,[1] Dalton Griner,[1] Roger Harrison,[2] Alex H. Reid,[3] Mark Transtrum,[1] and Karine Chesnel[1,a)]

AFFILIATIONS

[1]Department of Physics and Astronomy, Brigham Young University, Provo, Utah 84602, USA
[2]Department of Chemistry and Biochemistry, Brigham Young University, Provo, Utah 84602, USA
[3]SIMES, SLAC National Accelerator Laboratory, Menlo Park, California 94025, USA

Note: This paper was presented at the 2019 Joint MMM-Intermag Conference.
[a)]**Corresponding author:** Karine Chesnel, kchesnel@byu.edu

ABSTRACT

Magnetic nanoparticles are increasingly used in nanotechnologies and biomedical applications, such as drug targeting, MRI, bio-separation. Magnetite (Fe_3O_4) nanoparticles stand to be effective in these roles due to the non-toxic nature of magnetite and its ease of manufacture. To be more effective in these applications, a greater understanding of the magnetic behavior of a collection of magnetite nanoparticles is needed. This research seeks to discover the local magnetic ordering of ensembles of magnetite nanoparticles occurring under various external fields. To complete this study, we use x-ray resonant magnetic scattering (XRMS). Here we discuss the modeling of the magnetic scattering data using a one-dimensional chain of nanoparticles with a mix of ferromagnetic, anti-ferromagnetic, and random orders. By fitting the model to the experimental data, we extracted information about the magnetic correlations in the nanoparticle assembly.

I. INTRODUCTION

Magnetic nanoparticles (NPs) are a vital part of many applications in biomedicine and other nanotechnologies.[1] There is a growing interest in NP for drug targeting, MRI, and bio-separation applications.[2–4] Magnetite (Fe_3O_4) NPs have potential as contrasting agents[5] in MRI imaging because they are non-toxic and easy to manufacture.[6] Because magnetite is a ferrimagnetic iron oxide that is naturally occurring and readily found in minerals, it is also a viable candidate in applications requiring large quantities of particles such as bio-separation and drug targeting. Magnetite's bulk properties have been widely studied,[7,8] but a better understanding of magnetite NPs, rather than bulk material, is needed for the substance to be effective in the applications mentioned above.

This work seeks to model the inter-particle magnetic ordering in magnetite NP assemblies. When their size is below about 100 nm, the magnetite NPs are individually magnetic monodomains. A collection of these NPs shows a superparamagnetic behavior, where the individual nanomagnets are randomly oriented and only align if an external magnetic field is applied. When cooled down, the NP assembly undergoes a magnetic transition characterized by the blocking temperature T_B above which the system is superparamagnetic and below which it is magnetically blocked. In our previous work, we have evaluated T_B on assemblies of 5-11 nm magnetite NPs using field cooling (FC) and zero-field-cooling (ZFC) measurements and established that T_B drastically depends on the particle size, increasing from about 28 K for the 5 nm NPs to about 170 K for the 11 nm NPs.[9] The drastic change of T_B suggests that at the nanoscale, inter-particle correlations strongly depend on particle size. Magnetometry FC-ZFC measurements however only provide information about the net magnetization M of the material, so alternate experimental techniques are necessary to directly probe the nanoscale

magnetic correlations. Small Angle Neutron Scattering (SANS) has allowed probing the magnetic morphology and magnetic canting effects in large quantities of magnetite NPs.[10,11] Because our samples consist of single layers of NPs, we were unable to use the standard neutron scattering techniques. Instead, we use x-ray magnetic scattering, exploiting polarized x-rays, tuned to resonant energies for the material, thus providing a magneto-optical contrast sufficient to access magnetic information.[12]

Resonant x-ray scattering provides an adequate tool to probe nanoscale magnetic correlations.[13,14] When x-rays are tuned to resonance edges of a magnetic element, here the Fe-L_3 edge, the magneto-optical contrast in the absorbed and scattered light gets enhanced, thus allowing the extraction of the magnetic signal from the charge signal. Our x-ray magnetic circular dichroism (XMCD) measurements on 5-11 nm magnetite NPs[13] have shown that for all sizes, the orbital magnetic moment is quenched and most of the magnetization in the NPs is supported by the spin magnetic moment. We have also seen little dependence of the magnetization per unit Fe_3O_4 on particle size. Our subsequent x-ray resonant magnetic scattering (XRMS) measurements[14] have demonstrated that x-ray scattering can be used to access spatial magnetic orderings at the nanoscale. In particular, by comparing XRMS signals collected at opposite helicities of the x-ray light, one can extract a scattering profile that provides information about inter-particle magnetic correlations in the NP assembly. We found that the shape of the XRMS signal and its evolution as a function of a magnetic field, applied in-situ, were different for the 5 nm and the 11 nm particle sizes. The visual analysis of the XRMS data suggests that while 5 nm NPs show a pure superparamagnetic behavior, inter-particle magnetic correlations may exist for the bigger, 11 nm particles, even at high temperature above T_B. To interpret these experimental results, we develop here a modeling of the magnetic correlations in the NP assembly.

Our main objective with this modeling work is to unveil the magnetic orderings present in the material when the applied magnetic field H is reduced to low values approaching zero. How do the nanomagnets behave at low H? Do they tend to take random orientations or do they adopt a specific arrangement? The magnetometry measurements indicate that when $H \approx 0$, $M \approx 0$. However, this information does not allow to make conclusions on the nanoscale magnetic ordering as both antiferromagnetic (AF) and random arrangements lead to $M = 0$. Only the XRMS scattering data allows to discriminate between the two components. With this preliminary modeling, we aim to show the possibility to model inter-particle magnetic correlations in the magnetite NP assemblies by using XRMS data and discriminate between magnetic order and randomness at low magnetic field.

In this paper, we will concentrate on one size of magnetite NP, 11 nm, for which magnetic correlations appear to be present.[14] In the following sections, we first describe the XRMS data collected on a specific 11 nm NP assembly, show the charge and magnetic components of the scattering signal. We then describe our model, consisting of a one-dimensional chain of NPs, the associated charge and magnetic density profiles, and the simulated XRMS signal based on this model. We then explain how our fitting procedure is performed and show some first successful results from the fit.

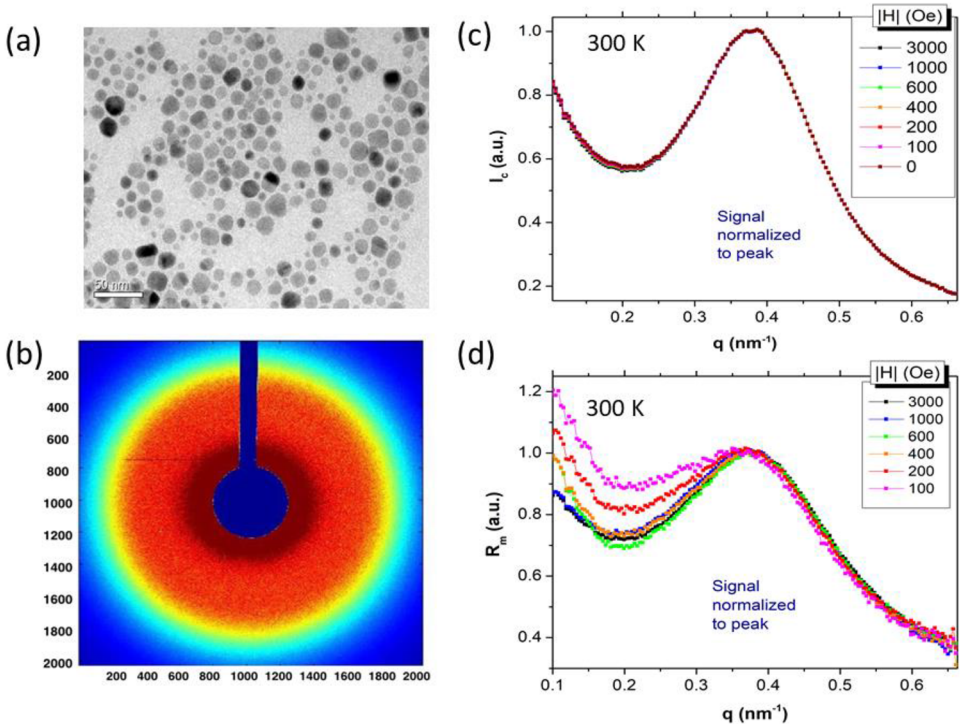

FIG. 1. Experimental data (a) TEM image of a Fe_3O_4 NP assembly for which the average particle size is 11 nm. (b) XRMS scattering pattern produced by the 11 nm Fe_3O_4 NP assembly at 300 K, at the Fe-L_3 edge (708 eV). (c) Normalized intensity radial profile obtained after azimuthal integration, showing the charge component $I_c = I_+ + I_-$ for various magnitudes of field H. (d) Normalized magnetic ratio profile $R_m = \frac{I^+ - I^-}{\sqrt{I^+ + I^-}}$ for various magnitudes of field H. All the profiles are normalized to the main peak for comparison purposes.

II. X-RAY MAGNETIC SCATTERING DATA

The experimental data used for our model consists of XRMS scattering patterns measured on a single layer of 11 nm magnetite NPs at room temperature 300 K (above T_B). To collect this data, the NPs were deposited on silicon nitride (Si_3N_4) membranes. Once deposited, the particles tend to self-assemble and form islands of monolayers with hexagonal lattices, as seen on the TEM image in Fig. 1a. From this TEM image, we evaluated the average particle size D and its standard of deviation, here $D = 11 \pm 4.6$ nm. Under x-ray illumination, the NPs produced a scattering XRMS pattern, in the shape of a ring, as shown Fig. 1b. The isotropic ring-like shape is due to averaging many NP arrays of different orientations (similar to powder diffraction). The radius of the ring provides an estimate of the average inter-particle distance p^*, here about 16.5 nm, implying an average gap L of about 5.5 nm between neighboring particles (assuming $p^* = D + L$).

To collect the XRMS patterns presented in this paper, the energy of the polarized x-rays was tuned to the Fe-L_3 resonance edge at around 708 eV. The XRMS signal contains a mix of charge scattering and magnetic scattering.[15,16] To follow the evolution of the signal throughout the magnetization process, XRMS patterns were collected at various in-situ applied magnetic fields H, ranging from -3000 Oe to +3000 Oe. It is expected that while the charge component of the scattering signal remains unchanged, the magnetic component may change when the magnetic field is varied.

To quantitatively follow the evolution of the scattering signal with magnetic field H, an azimuthal integration is applied on the 2D XRMS images so to produce a 1D scattering profile $I(q)$, as shown in Fig. 1c, where I is the integrated intensity and q is the distance from the center of the ring. The resulting profile $I(q)$ shows a peak, whose position q^* indicates the average inter-particle distance $p^* = 2\pi/q^*$. To quantitatively extract the charge and magnetic components from the scattering signal, the intensities measured in opposite helicities of the light $I_+(q)$ and $I_-(q)$ are compared. Given certain approximations,[14–16] our charge and magnetic components are respectively represented by the quantities I_c (charge intensity) and R_m (magnetic ratio):

$$I_c = I_+ + I_- \tag{1}$$

$$R_m = \frac{I^+ - I^-}{\sqrt{I^+ + I^-}} \tag{2}$$

In Fig. 1c, $I_c(q)$ is plotted for various magnitudes of magnetic field H ranging from 3000 Oe down to zero, after normalization. Remarkably, $I_c(q)$ is unchanged when the field is varied. In Fig. 1d, $R_m(q)$ is plotted for various magnitudes of magnetic field H ranging from 3000 Oe down to 100 Oe, after normalization to the main peak. The value at $H = 0$ is left off because at that point $M \approx 0$ and the magnetic signal R_m, which scales with M, is also ≈ 0. Interestingly, and unlike for $I_c(q)$, the shape of $R_m(q)$ visibly changes when the field is varied, confirming the magnetic nature of $R_m(q)$.

The main peak in $R_m(q)$ is located at the same position q^* than the peak in $I_c(q)$, suggesting a magnetic period p_m identical to the structural period p^*. That magnetic period corresponds to a ferromagnetic (FM) order, where the nanomagnets are all aligned. At high field, H = +3000 Oe, when a large portion of the nanomagnets is aligned with the external field, this FM peak is more pronounced. When the field is decreased down to H = +100 Oe, the peak is less pronounced, suggesting the occurrence of magnetic periodicities other than the FM order. In particular, the signal at $q < q^*$ increases, suggesting magnetic periods larger than p^*. The signal at $q < q^*$ includes the antiferromagnetic (AF) order, where neighboring nanomagnets alternate in direction, leading to an average period $p_m = 2p^*$. By modeling the measured scattering signal, we hope to extract quantitative estimates for the various magnetic ordering contributions, including the FM and AF orders.

III. FITTING THE DATA

A. Description of the model

Our model is constructed on the premise that the combined magnetometry and XRMS signals contain sufficient enough information to draw conclusions regarding the magnetic ordering of magnetite NPs. The model simultaneously fits against the two quantities defined in Section II, which are I_c (charge intensity) and R_m (magnetic ratio). Fitting I_c provides information about the structure of the NP assembly, while fitting R_m provides information about the magnetic correlations, based on the structural information. The quantification of the various magnetic orders in the material also utilizes magnetometry data, in particular the net magnetization M at various magnetic fields H, which allows assessing the amount of FM order.

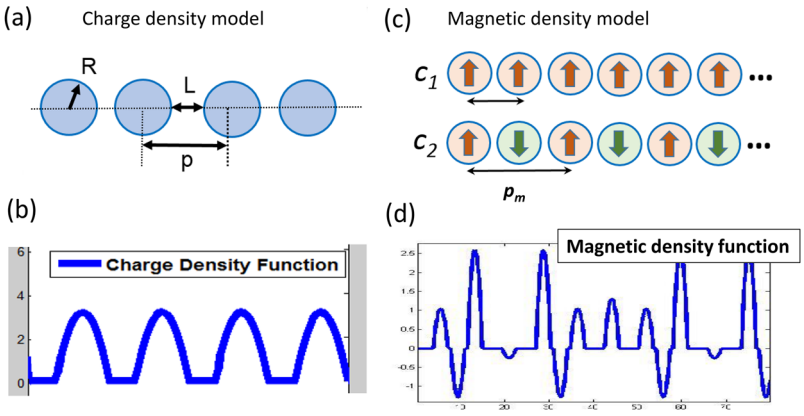

FIG. 2. Visuals of the model (a) Chain of nanoparticles where the structural parameters are the radius R and the separation distance L with associated period $p = 2R + L$; (b) Charge density function $\Phi_i(r, \theta)$ for the chain (a); (c) Representations of the ferromagnetic (FM) and antiferromagnetic (AF) orders. (d) Magnetic density function $M(r, \theta)$ resulting from combining FM and AF orders.

TABLE I. Listing of the 12 parameters $\boldsymbol{\theta}$ used in our fit. All parameters were allowed to vary per the parameter search algorithm discussed in Section III B.

Θ_1	mean particle separation (L_0)
Θ_2	charge signal offset
Θ_3	magnetic signal offset
Θ_4	AF component (c_2)
Θ_5	charge peak magnitude
Θ_6	magnetic central (q = 0) peak height
Θ_7	charge central (q = 0) peak height
Θ_8	FM correlation length (σ_{FM})
Θ_9	AFM correlation length (σ_{AFM})
Θ_{10}	Charge peak width
Θ_{11}	magnetic central (q = 0) peak width
Θ_{12}	charge central (q = 0) peak width

The fitting signal is constructed of 1-dimension chains of NPs, as illustrated in Fig. 2a. The length of the chain is typically around $N = 100$ particles. We account for the statistical variance observed in the TEM images for the particle radius (R) and for the inter-particle space (L) by uniformly sampling from a Gaussian distribution whose average values ($R_0 = 5.5$ nm, $L_0 \approx 5.5$ nm) and standard deviations ($\sigma_R = 2.3$ nm, $\sigma_L = 0.85$ nm) correspond to what is measured from the TEM images (Fig. 1.a) or left to vary as a parameter in the case L_0. We use the sampled value and its respective probability to construct the charge density function for a chain of NPs, $\Phi(r, \boldsymbol{\theta})$ where r represents the particle position and $\boldsymbol{\theta}$ are the model parameters. Table I shows a detailed listing of these parameters, which are all fitted.

An example of charge density function $\Phi(r, \boldsymbol{\theta})$ for a given particle size R and spacing L is showed in Fig. 2b. The overall (averaged) charge density signal $C(r, \boldsymbol{\theta})$ is then given by:

$$C(r, \boldsymbol{\theta}) = \sum_i P(i)\phi_i(r, \boldsymbol{\theta}) \tag{3}$$

where $\Phi_i(r, \boldsymbol{\theta})$ represents one particular chain constructed from the Gaussian distribution value (using a radius R_i and spacing L_i), $P(i)$ is the probability of that value occurring (using the Gaussian distribution variances σ_R and σ_L), and $\boldsymbol{\theta}$ are the model parameters.

Once the charge density function $C(r, \boldsymbol{\theta})$ is constructed, a magnetic density function $M(r, \boldsymbol{\theta})$ is constructed for different types of magnetic orders, namely the ferromagnetic (FM) and the antiferromagnetic (AF) orders. The corresponding magnetic density functions, $FM(r, \boldsymbol{\theta})$ and $AF(r, \boldsymbol{\theta})$ are basically constructed based of the individual charge density functions $\phi_i(r, \boldsymbol{\theta})$ by assigning a spin of a certain direction (up/down) to each NP, as follows:

$$FM(r, \boldsymbol{\theta}) = \sum_i \text{spinFM}_i(r)P(i)\phi_i(r, \boldsymbol{\theta})$$
$$AF(r, \boldsymbol{\theta}) = \sum_i \text{spinAF}_i(r)P(i)\phi_i(r, \boldsymbol{\theta})$$

For the FM order all the spins are aligned in the same direction, so $FM(r, \boldsymbol{\theta}) = C(r, \boldsymbol{\theta})$. For the AF order, $\text{spinAF}_i(r)$ includes an alternation of spin up (+1) and spin down (-1), as illustrated in Fig. 2c. The resulting average magnetic density function $M(r, \boldsymbol{\theta})$ is a combination of the two orders:

$$M(r, \boldsymbol{\theta}) = c_1\mathcal{N}_{FM}(r, \boldsymbol{\theta})FM(r, \boldsymbol{\theta}) + c_2\mathcal{N}_{AF}(r, \boldsymbol{\theta})AF(r, \boldsymbol{\theta})$$

where $\mathcal{N}_{FM}(r, \boldsymbol{\theta})$ and $\mathcal{N}_{AF}(r, \boldsymbol{\theta})$ are normal Gaussian distributions with standard deviations σ_{FM} and σ_{AF} to account for the FM and AF correlation lengths, respectively. The coefficients c_1 and c_2 represent the proportions (as percentages) of the FM and AF orders, respectively. Because only the FM order contributes to the net magnetization M of the material (the AF order leads to an average of $M \approx 0$), the value for c_1 is set by the normalized magnetization: $c_1 = M/M_s$ where M is the measured net magnetization at a given magnetic field, and M_s is the magnetization at saturation (maximum value for M). c_2 is one of the model parameters $\boldsymbol{\theta}$ (see Table I) and is evaluated by the fit.

The scattering intensity is derived as the norm square of the scattering amplitude, a complex quantity that includes Fourier transforms of the charge and magnetic density functions. Our simulated scattering signal is therefore computed via Fourier transforming $C(r, \boldsymbol{\theta})$ and $M(r, \boldsymbol{\theta})$:

$$\tilde{M}(q, \boldsymbol{\theta}) = \mathcal{F}T[M(r, \boldsymbol{\theta})]$$
$$\tilde{C}(q, \boldsymbol{\theta}) = \mathcal{F}T[C(r, \boldsymbol{\theta})]$$

These signals are then used in the following manner to fit against the charge and magnetic scattering data I_c and R_m:[13]

$$I_c = \left|\tilde{C}(q, \boldsymbol{\theta})\right|^2$$

$$R_m = \frac{\left|Re\left(\tilde{M}(q, \boldsymbol{\theta})\right)\left[\beta Re\left(\tilde{C}(q, \boldsymbol{\theta})\right) + \alpha Im\left(\tilde{C}(q, \boldsymbol{\theta})\right)\right] - Im\left(\tilde{M}(q, \boldsymbol{\theta})\right)\left[\alpha Re\left(\tilde{C}(q, \boldsymbol{\theta})\right) - \beta Im\left(\tilde{C}(q, \boldsymbol{\theta})\right)\right]\right|}{\left|\tilde{C}(q, \boldsymbol{\theta})\right|}$$

where α and β are the real and imaginary parts of a charge scattering factor, $f = \alpha + i\beta$, whose tabulated value depends on the scattering atom (here Fe) and the energy of the x-rays (here ~ 708 eV).[17] *Re* and *Im* represents the real and imaginary parts of $\tilde{C}(q, \boldsymbol{\theta})$ and $\tilde{M}(q, \boldsymbol{\theta})$ which are both complex quantities. While the modeled I_c signal only uses $\tilde{C}(q, \boldsymbol{\theta})$, the modeled R_m signal uses both $\tilde{C}(q, \boldsymbol{\theta})$ and $\tilde{M}(q, \boldsymbol{\theta})$, necessitating fitting both quantities simultaneously.

B. Description of the fitting approach

Our fitting approach utilizes a global fit of both the I_c and R_m experimental data. We make use of a Levenberg-Mardquardt algorithm[18,19] to solve the non-linear least squares learning problem which determines the parameter values that minimize the 2-norm between the experimental data Y and the fitted data $G(\boldsymbol{\theta})$ for both I_c

and R_m simultaneously:

$$\boldsymbol{\theta}^* = \text{argmin}_\theta \| G(\boldsymbol{\theta}) - Y \|_2$$

where $\boldsymbol{\theta}^*$ are the 12 parameter values that minimize the 2-norm between the fit $G(\boldsymbol{\theta})$ and the data Y.

We determine the model's standard error σ using the Fisher information matrix (FIM).[20] The FIM can be constructed using the model's Jacobian matrix, which is calculated in the process of the Levenberg-Marquardt algorithm:

$$FIM = \frac{1}{\sigma^2} J'J$$

$$\sigma^2 = \frac{\chi^2}{m-n}, \chi^2 = \sum_n \left(Y_n - G(\theta^*)_n \right)^2$$

where J is the Jacobian, χ^2 is the sum of the residuals squared, calculated in the canonical way, m and n are the number of data points, and the number of parameters, respectively. The square root of diagonal elements of the covariant matrix, or the inverse FIM, comprises the standard error σ_i for each of the parameters θ_i

$$cov = FIM^{-1}$$

$$\sigma_i = diag(\sqrt{cov})_i$$

IV. RESULTS

We applied our fitting procedure to the entire set of XRMS patterns collected at 300 K on a 11 nm NP assembly, shown in Fig. 1, with an applied in-situ magnetic field H varying from + 3000 Oe down to – 3000 Oe. The associated charge scattering I_c and magnetic ratio R_m data used for the fit are shown in Fig. 1c,d. For each magnetic field value H, I_c and R_m were simultaneously fitted. An illustration of our data fitting is shown in Fig. 3a,b where the model is compared to the data, for the I_c signal (Fig. 3a) and the R_m signal (Fig. 3b) at H = -100 Oe. The model here extends through a wider range of q values, including a peak at q = 0 which we introduced in order to fit the diffuse scattering background.

Among all the fitted parameters $\boldsymbol{\theta}$, the ones susceptible to increase our understanding of the magnetic correlations are the percentage coverages for the FM order (c_1) and the AF order (c_2). Any remaining portion that is not FM nor AF is considered as magnetic randomness (R). The R proportion is $c_0 = 1 - c_1 - c_2$. Our fitting results for the coefficients c_0, c_1 and c_2 for the 11 nm NPs at 300 K are shown in Fig. 3c. At high magnetic field H = +3000 Oe, the FM component c_1 is predominant with a value as high as 90%, indicating that 90% of the nanomagnets are aligned with the external field. When the field H is decreased, the coefficient c_1 decreases accordingly, i.e., proportionally to the net magnetization M. The coefficient c_0 then progressively increases. When $H \approx$ +500 Oe, c_1 and c_0 become comparable, with $c_1 \approx$ 50% and $c_0 \approx$ 40%. When the field H is further decreased, c_1 continues to decrease, c_0 becomes predominant, and a small c_2 component emerges. At H = +100 Oe, the FM component has become minor ($c_1 \approx$ 20%) and the rest of the material is a mix of randomness ($c_0 \approx$ 50%) and AF order ($c_2 \approx$ 30%).

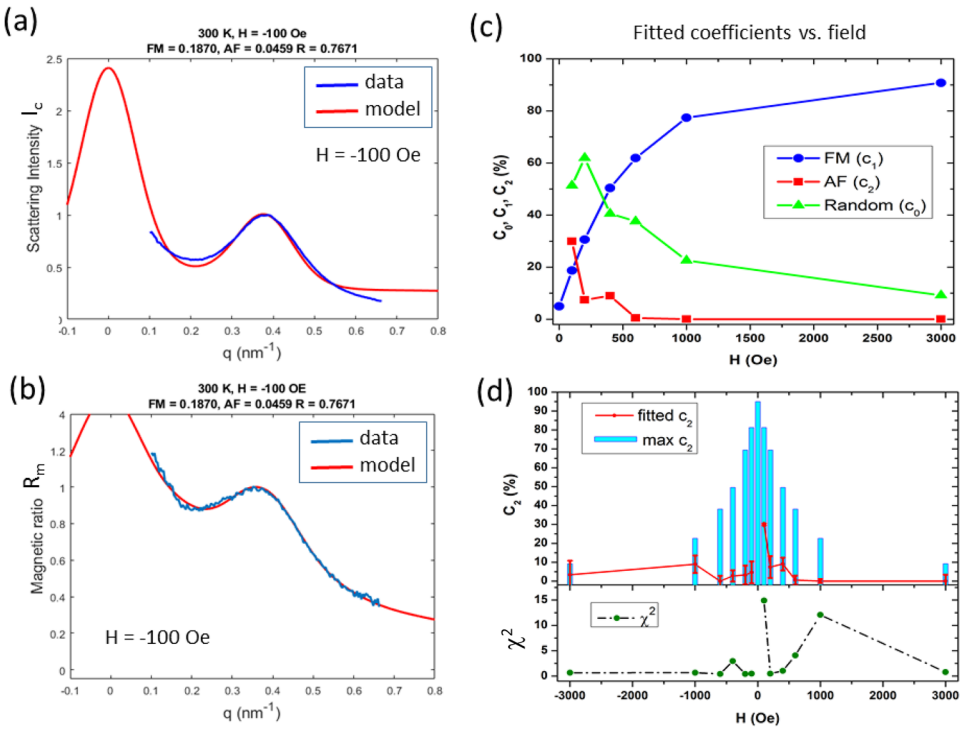

FIG. 3. Fitting results. (a-b) Example of fits performed at a field H = - 100 Oe, on (a) the charge scattering intensity I_c data and (b) the magnetic ratio R_m data; (c) Fitted coefficients (expressed as percentages) for the FM component (c_1), the AF component (c_2) and the random component (c_0) as a function of magnetic field H, for positive H; (d) Fitted AF coverage (c_2) including error bars at 95% confidence intervals for the whole range of magnetic fields (-3000 Oe, +3000 Oe). The blue bars indicate the possible range for c_2, the maximum value being set by $1 - c_1$ (c_0 = 0). Also plotted, the χ^2 values of the LM algorithm.

A similar study was applied to the negative side of the magnetization cycle ($H < 0$). In Fig. 3d, the fitted coefficient c_2 is plotted for the whole range of magnetic fields H = [- 3000 Oe, + 3000 Oe]. The graph includes error bars corresponding to the standard deviation for c_2 at 95% confidence intervals. Also in Fig. 3d, the range of possible values for c_2 is shown (blue bars) for each H point. The range [0, $c_{2,max}$] is set by $c_{2,max} = 1 - c_1$, that is when $c_0 = 0$ (no randomness) and the whole NP assembly is either FM or AF arranged.

Fig. 3d indicates that the fitted c_2 is found to be (within two standard deviations) in the allowed regions, but remains low compared to $c_{2,max}$. Also the χ^2 values plotted in Fig. 3d obtained for this particular set of data indicate that our model was better able to fit the negative branch of the applied field cycle. The fitted c_2 values show some variations between the negative side and the positive side of the magnetization cycle. This variation is largely due to the experimental error inherent to the data collection necessitating field and polarization switching of the synchrotron light. A reduction of the experimental error would likely improve the consistency and symmetry of the results between the ascending and descending branches. While the confidence intervals for the AF parameter may be too wide to make precise estimates in this particular set of data, the general trend of these confidence intervals to decrease with the applied field shows that the model performs better in the low field region.

In addition to the coefficients c_1 and c_2, other interesting fitted parameters are the FM and AFM correlation lengths, represented by the standard deviations σ_{FM} and σ_{AFM} in the normal Gaussian distributions used to build $M(r, \boldsymbol{\theta})$. The associated correlation length λ (in real space) may be derived from the standard deviation σ as follows: $\lambda = 2\sqrt{2}\,ln2\,\sigma \approx 2\sigma$. Table II lists the fitted results for these quantities. The fitted FM correlation length lies in the range 30-40 nm, while the fitted AFM correlation length lies around 14 nm, which is a very short range.

Overall, the behavior of c_2 indicates that while c_2 is very small, close to zero, at high magnetic fields H, its value tend to increase when H approaches zero. At $H = 0$, while the majority of the nanomagnets are randomly oriented, which is what is expected at $T > T_B$ when the material is superparamagnetic, a small portion of them may show some AF ordering. Next, it will be interesting to fit the XRMS data collected at lower temperatures $T < T_B$ and see how the inter-particle correlations may evolve as the system transitions into a blocked magnetic state.

TABLE II. Listing of the AFM and FM correlation lengths for the negative branch of the magnetization loop.

H (Oe)	σ_{FM} (nm)	λ_{FM} (nm)	σ_{AFM} (nm)	λ_{AFM} (nm)
-3000	18.81	36.87	7.266	14.24
-1000	18.67	37.34	7.244	14.20
-600	17.66	35.32	7.03	13.78
-400	17.25	34.50	7.22	14.15
-200	16.88	33.76	6.95	13.62
-100	15.46	30.92	7.16	14.03
0	20.70	41.40	6.62	12.97

V. CONCLUSION

In this paper, we have demonstrated the possibility to model inter-particle magnetic correlations in 2D assemblies of magnetic NPs by using x-ray scattering (XRMS) data, a non-traditional method, complementary to the traditional neutron scattering approaches. Our modeling of XRMS data collected on assemblies of 11 nm NPs at 300 K, shows that when approaching remanence ($H \approx 0$), the nanomagnets tend to randomly orient, but that a non-negligible anti-ferromagnetic component exist. This result confirms the superparamagnetic nature of the material at $T > T_B$. This fitting approach can next be applied to data collected at low temperature, $T < T_B$, when the material becomes magnetically blocked and study how inter-particle magnetic correlations evolve with T. This approach can also be applied to study the dependence of magnetic correlations on particle size and concentration in the self-assembly.

ACKNOWLEDGMENTS

We thank Dr Jeffrey Kortright for helpful discussions on the theory of x-ray resonant magnetic scattering. We thank the Office of Research and Creative Activities at Brigham Young University for funding this work.

REFERENCES

[1] N. A. Frey, S. Peng, K. Cheng, and S. Sun, "Magnetic nanoparticles: Synthesis, functionalization, and applications in bioimaging and magnetic energy storage," Chem. Soc. Rev. **38**, 2532–2542 (2009).
[2] S. Mornet, S. Vasseur, F. Grasset, and E. Duguet, "Magnetic nanoparticle design for medical diagnosis and therapy," J. Mater. Chem. **14**, 2161 (2004).
[3] E. Duguet, S. Vasseur, S. Mornet, and J. M. Devoiselle, "Magnetic nanoparticles and their applications in medicine," Nanomedicine **1**(2), 157 (2006).
[4] J. H. Gao, H. Gu, and B. Xu, "Multifunctional magnetic nanoparticles: Design, synthesis and biomedical applications," Acc. Chem. Res. **42**(8), 1097 (2009).
[5] Y.-W. Jun, J. H. Lee, and J. Cheon, "Chemical design of nanoparticle probes for high-performance magnetic resonance imaging," Angew. Chem. Int. Ed. **47**, 5122–5135 (2008).
[6] A. Ito, M. Shinkai, H. Honda, and T. Kobayashi, "Medical application of functionalized magnetic nanoparticles," J. Biosci. Bioeng. **100**, 1 (2005).
[7] E. J. Verwey, "Electronic conduction of magnetite (Fe_3O_4) and its transition point at low temperatures," Nature (London) **144**, 327 (1939).
[8] M. E. Fleet, "The structure of magnetite," Acta Crystallogr.B: Struct, Crystallogr. Cryst. Chem. **37**, 917–920 (1981).
[9] K. Chesnel, M. Trevino, Y. Cai, J. M. Hancock, S. J. Smith, and R. G. Harrison, "Particle size effects on the magnetic behaviour of 5 to 11 nm Fe_3O_4 nanoparticles coated with oleic acid," J. Phys.: Conf. Series **521**, 012004 (2014).
[10] K. L. Krycka, R. A. Booth, C. R. Hogg, Y. Ijiri, J. A. Borchers, W. C. Chen, S. M. Watson, M. Laver, T. R. Gentile, L. R. Dedon, S. Harris, J. J. Rhyne, and S. A. Majetich, "Core-shell magnetic morphology of structurally uniform magnetite nanoparticle," Phys. Rev. Lett. **104**, 207203 (2010).
[11] K. L. Krycka, J. A. Borchers, R. A. Booth, Y. Ijiri, K. Hasz, J. J. Rhyne, and S. A. Majetich, "Origin of surface canting within Fe_3O_4 nanoparticles," Phys. Rev. Lett. **113**(14), 147203 (2014).
[12] K. Chesnel, J. J. Turner, M. Pfeifer, and S. D. Kevan, "Probing complex materials with coherent soft x-rays," Appl. Phys. A **92**(3), 431–437 (2008).
[13] Y. Cai, K. Chesnel, M. Trevino, A. Westover, R. G. Harrison, J. M. Hancock, S. Turley, A. Scherz, A. Reid, B. Wu, C. Graves, T. Wang, T. Liu, and H. Dürr, "Orbital and spin moments of 5 to 11 nm Fe_3O_4 nanoparticles measured via x-ray magnetic circular dichroism," J. Appl. Phys. **115**(17), 17B537 (2014).

[14]K. Chesnel, D. Griner, D. Smith, Y. Cai, M. Trevino, B. Newbold, T. Wang, T. Liu, E. Jal, A. H. Reid, and R. G. Harrison, "Unraveling magnetic ordering in Fe_3O_4 nanoparticle assemblies via x-rays," Magnetochemistry **4**, 42–58 (2018).
[15]J. B. Kortright, O. Hellwig, K. Chesnel, S. Sun, and E. E. Fullerton, "Interparticle magnetic correlations in dense Co nanoparticle assemblies," Phys. Rev. B **71**, 012402 (2005).
[16]J. Kortright, M. Rice, and R. Carr, "Soft-x-ray Faraday rotation at Fe $L_{2,3}$ edges," Phys. Rev. B **51**, 10240 (1995).
[17]CXRO data base for X-ray Interactions with Matter (http://henke.lbl.gov).
[18]K. Levenberg, "A method for the solution of certain non-linear problems in least squares," Quarterly of Applied Mathematics. **2**, 164–168 (1944).
[19]D. Marquardt, "An algorithm for least-squares estimation of nonlinear parameters," SIAM Journal on Applied Mathematics. **11**(2), 431–441 (1963).
[20]L. Alexander, M. Marsman, J. Verhagen, R. Grasman, E.-J. Wagenmakers, "A tutorial on Fisher information," eprint arXiv:1705.01064 [math.ST].